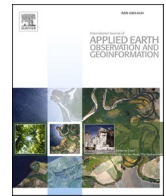




Contents lists available at ScienceDirect

International Journal of Applied Earth Observations and Geoinformation

journal homepage: www.elsevier.com/locate/jag

Evaluation of the AVHRR surface reflectance long term data record between 1984 and 2011

Andres Santamaria-Artigas^{a,b,*}, Eric F. Vermote^b, Belen Franch^{a,c}, Jean-Claude Roger^{a,b}, Sergii Skakun^{a,b}

^a Department of Geographical Sciences, University of Maryland, 2181 LeFrak Hall, College Park, MD 20740, USA

^b NASA Goddard Space Flight Center, 8800 Greenbelt Rd, Greenbelt, MD 20771, USA

^c University of Valencia, C/Catedrático Agustín Escardino, Paterna, Valencia 46980, Spain

ARTICLE INFO

Keywords:

AVHRR
LTDR
TM5
Surface Reflectance
BRDF
SBAF

ABSTRACT

The long-term data record (LTDR) from the Advanced Very High-Resolution Radiometer (AVHRR) provides daily surface reflectance with global coverage from the 1980s to present day, making it a unique source of information for the study of land surface properties and their long-term dynamics. Surface reflectance is a critical input for the generation of products such as vegetation indices, albedo, and land cover. Therefore, it is of utmost importance to quantify its uncertainties to better understand how they might propagate into downstream products. Due to the prolonged length of the surface reflectance LTDR and previous unavailability of a well calibrated reference, no comprehensive evaluation of the complete record has been reported so far. Recently, the United States Geological Survey (USGS) began production of surface reflectance datasets from the Landsat 4-8 satellites, which provide a suitable reference against which the LTDR can be compared to. In this study, we evaluate the LTDRV5 between 1984 and 2011 using surface reflectance data from the Landsat-5 Thematic Mapper (TM5) Collection-1 as a reference. Data from TM5 was obtained from over 740,000 globally distributed scenes which gave a representative set of land surface types and atmospheric conditions. Differences due to observation geometry were accounted for using the Vermote-Justice-Breon (VJB) Bidirectional Reflectance Distribution Function (BRDF) normalization method to adjust the AVHRR surface reflectance to TM5 observation conditions; the spectral response differences were minimized using spectral band adjustment factors (SBAFs) derived from the Earth Observing One (EO-1) Hyperion atmospherically corrected hyperspectral spectra. The performance of the AVHRR record is reported in terms of the accuracy, precision, and uncertainty (APU). Results show that the LTDR performance is close or within the combined uncertainty specification of $0.071\rho + 0.0071$, where ρ is the estimated reflectance.

1. Introduction

Satellite remote sensing is an essential source of quantitative information for the global monitoring and study of land surface properties and their long-term dynamics. Long term records from satellite observations allow us to study and better understand extreme events and changes in our planet to an extent that would not be possible otherwise (Potapov et al., 2015; Skakun et al., 2016; Song et al., 2018a; Zhang, 2015). Amongst long-term satellite records, the one from the Advanced Very High-Resolution Radiometer (AVHRR) on board the NOAA polar-orbiting environmental satellites (POES) provides the longest time-

series of daily global satellite measurements, which starts in the early 1980 s and continues to the present day.

The surface reflectance long-term data record (LTDR) from AVHRR is an ongoing effort to generate a consistent climate record of atmospherically corrected daily observations with global coverage. The LTDR is generated using data from two versions of the AVHRR sensor onboard seven POES platforms: AVHRR/2, onboard platforms N07, N09, N11, and N14 (referred to as pre-KLM); and AVHRR/3, onboard platforms N16, N18, and N19 (KLM). Throughout the years, the LTDR team has developed a processing chain that includes an accurate geolocation with an error lower than one pixel (Franch et al., 2017); the monitoring of

* Corresponding author at: Department of Geographical Sciences, University of Maryland, 2181 LeFrak Hall, College Park, MD 20740, USA.

E-mail addresses: asantam@umd.edu (A. Santamaria-Artigas), eric.f.vermote@nasa.gov (E.F. Vermote), belen.franch@uv.es (B. Franch), roger63@umd.edu (J.-C. Roger), skakun@umd.edu (S. Skakun).

<https://doi.org/10.1016/j.jag.2021.102317>

Received 16 September 2020; Received in revised form 7 January 2021; Accepted 5 February 2021

0303-2434/© 2021 The Author(s). Published by Elsevier B.V. This is an open access article under the CC BY-NC-ND license

(<http://creativecommons.org/licenses/by-nc-nd/4.0/>).

sensor degradation using observations of clouds and ocean (Vermote and Kaufman, 1995), and desert sites (Vermote and Saleous, 2006a); cloud masking from albedo thresholds derived from Moderate Resolution Imaging Spectroradiometer (MODIS) information; atmospheric correction based on the Second Simulation of the Satellite signal in the Solar Spectrum (6S) radiative transfer code (Vermote et al., 1997); and normalization of directional reflectance using the Vermote-Justice-Breon (VJB) method (Vermote et al., 2009). The LTDR record has been used for studies at both regional and global scales, and for areas such as agricultural yield estimation (Franch et al., 2017), agricultural drought risk quantification (Skakun et al., 2016), long-term global land change mapping (Song et al., 2018a); and the estimation of parameters such as albedo (Song et al., 2018), and Leaf Area Index (LAI) and Fraction of Photosynthetically Active Radiation (FAPAR) (Claverie et al., 2016).

Quality of the surface reflectance record should be the highest possible, and the assessment of its uncertainties is crucial to understand the record's potential and limitations, and how the uncertainties might propagate to downstream products. While the surface reflectance LTDR has been widely used in the literature, previous studies have focused on either evaluating the calibration of top-of-atmosphere (TOA) values (Bhatt et al., 2016; Heidinger et al., 2002; Li et al., 2014) or evaluating surface reflectance values for only a particular set of POES platforms (Franch et al., 2017; Vermote and Kaufman, 1995; Vermote and Saleous, 2006a). Hence, no comprehensive evaluation of the complete surface reflectance record has been carried out so far. Nowadays, data from MODIS is routinely used to evaluate the surface reflectance performance of the most recent AVHRR sensors (Franch et al., 2017). While MODIS provides a well calibrated reference dataset, with daily global coverage, a robust atmospheric correction, and uncertainties lower than $0.05\rho + 0.005$ (where ρ is the surface reflectance), its data is only available since 2000 for Terra and 2002 for Aqua, which leaves over 19 years of record without a consistent surface reflectance reference.

In recent years, the United States Geological Survey (USGS) began production of surface reflectance products from Landsat 4, 5, 7, and 8 (Ju et al., 2012; Masek et al., 2006; Vermote et al., 2016), providing a long-term 16-day dataset at 30 m spatial resolution (<https://www.usgs.gov/land-resources/nli/landsat/landsat-collection-1-surface-reflectance>). Data from the Landsat-5 Thematic Mapper (TM5) sensor spans a period of over 27 years, which covers most of the LTDR record lifetime. While it was initially shown that the internal calibration (IC) system of TM5 was not particularly stable (Chander and Markham, 2003), the bands calibration has been routinely updated based on the detectors response to the IC, the continuous observation of pseudo-invariant sites, and the cross-calibration with Landsat-7 ETM+ (Chander et al., 2009, 2004; Chander and Markham, 2003). These efforts have achieved a radiometric calibration uncertainty of around 7% for the at-sensor radiance (Markham and Helder, 2012). The surface reflectance product provided by USGS is generated using the Landsat Ecosystem Disturbance Adaptive Processing System (LEDAPS) (Masek et al., 2006). LEDAPS processing involves the calibration of images using revised coefficients and the atmospheric correction based on the 6S radiative transfer code. Performance of the LEDAPS TM5 surface reflectance product was shown to be better than specification of $0.071\rho + 0.0071$ in terms of surface reflectance uncertainty (Claverie et al., 2015). This record provides a unique opportunity for cross-comparison and evaluation of the AVHRR surface reflectance LTDR.

In this work, we present the first comprehensive evaluation of the AVHRR surface reflectance LTDR. For this, we use globally distributed LEDAPS TM5 surface reflectance data between 1984 and 2011 as a well-calibrated reference. To this extent, we implement an evaluation methodology that accounts for directional effects using the VJB method, and for spectral differences using spectral adjustment factors derived from EO-1/Hyperion hyperspectral data. The AVHRR record performance is reported in terms of the accuracy, precision, and uncertainty metrics (APU) (Vermote and Kotchenova, 2008), which are evaluated in

terms of their dependence to surface reflectance magnitude, land cover, temporal evolution, spatial distribution, and seasonality.

2. Materials and methods

2.1. AVHRR surface reflectance

In this study, we evaluate the AVHRR surface reflectance Long Term Data Record (LTDR) V5 (Franch et al., 2017) generated from Global Area Coverage AVHRR L1b data. The LTDR spans the period between 1981 to the present day and provides daily BRDF-normalized observations at spatial resolution of $0.05^\circ \times 0.05^\circ$ in the Climate Modeling Grid (CMG). The surface reflectance product includes information for 5 spectral channels, solar and view zenith angles, relative azimuth angles, and quality assessment. For this study, we use surface reflectance from the red (0.58–0.68 μm) and near infrared (0.72–1.10 μm) channels, the solar zenith, view zenith, and relative azimuth angles, and the quality layer, which was used to remove pixels contaminated by clouds or other atmospheric effects and analyze only those with the highest quality. The LTDR V5 surface reflectance products were obtained from <https://ltdr.modaps.eosdis.nasa.gov>.

2.2. Landsat-5 TM surface reflectance

Surface reflectance from the Landsat-5 Thematic Mapper sensor (TM5) was used as a reference to evaluate the AVHRR record. TM5 acquired images between 1984 and 2012, making it the longest operating Earth observation satellite. Data from TM5 has a temporal resolution of 16 days and a spatial resolution of 30 m. We used data from over 740,000 scenes of surface reflectance generated by LEDAPS (Masek et al., 2006) from terrain corrected L1TP top-of-atmosphere products (Collection-1, Tier-1). The spatial distribution of scenes is shown in Fig. 1, and the temporal distribution of scenes is shown in Fig. 2. The method for scene selection is explained on Section 3.1. For this study, we use surface reflectance from the red (0.63–0.69 μm) and near infrared (0.76–0.90 μm) channels, and quality information from the pixel quality, radiometric saturation, and atmospheric opacity layers. Evaluation of the TM5 LEDAPS surface reflectance found that it performed better than $0.071\rho + 0.0071$ (Claverie et al., 2015). The TM-5 Collection-1 Tier-1 surface reflectance products were downloaded from Google Earth Engine (https://developers.google.com/earth-engine/datasets/catalog/LANDSAT_LT05_C01_T1_SR).

2.3. Landsat-5 TM per-pixel angles

The TM5 surface reflectance product metadata provides information on the sun elevation and azimuth angles for the center of the scene but gives no information on the observation zenith and azimuth angles. With the purpose of having a better description of the solar and observation geometric characteristics of each scene, we computed the per-pixel solar zenith, solar azimuth, view zenith, and view azimuth angles using routines made available by USGS (<https://www.usgs.gov/land-resources/nli/landsat/solar-illumination-and-sensor-viewing-angle-coefficient-files>). These routines read an angle coefficient file unique to each scene and processes it using the Landsat Image Assessment System Geometric Libraries (Lee et al., 2004).

2.4. Hyperion surface reflectance spectra

In this study, spectral band adjustment factors (SBAF) between AVHRR and TM5 were derived from a set of more than 100,000 hyperspectral surface reflectance spectra acquired by the Hyperion (H0) spectrometer onboard the Earth Observer-1 (EO-1) satellite. Hyperion is a hyperspectral imager that acquires data from 198 calibrated bands in the range of 400 to 2500 nm with a ~ 10 nm spectral resolution and 30 m spatial resolution (Pearlman et al., 2003).

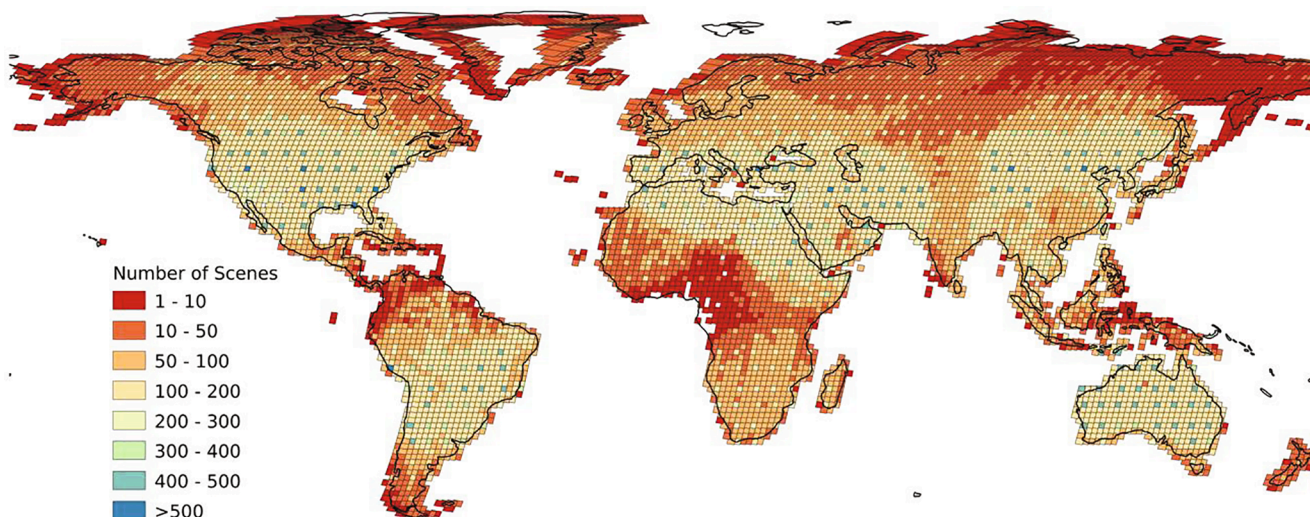


Fig. 1. Global distribution of Landsat-5 TM scenes used for evaluation.

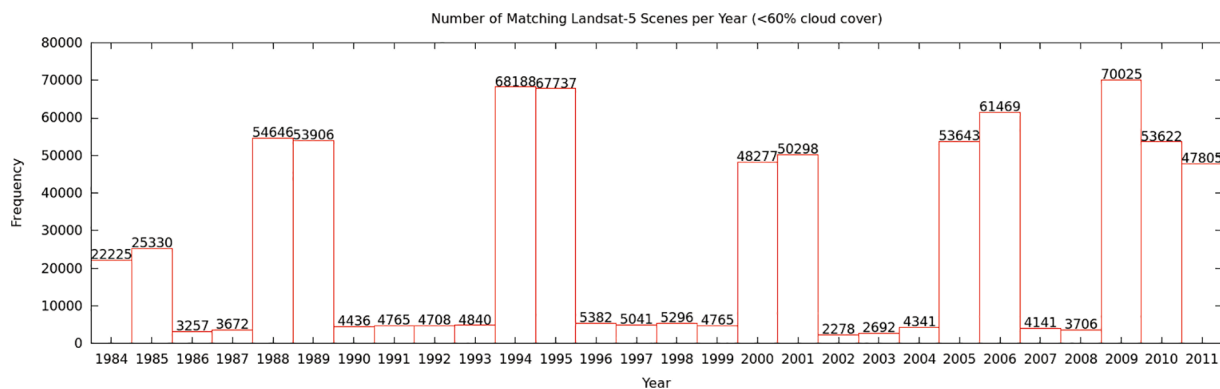


Fig. 2. Number of matching of Landsat-5 TM scenes per year.

For the purpose of deriving SBAFs over a wide range of conditions, data from two readily available surface reflectance data sets collected over Australia between 2001 and 2010 (Broomhall, 2012) and the Amazon rainforest between 2002 and 2005 (Chambers, 2012) were used. In total, 152 H0 granules were included for the derivation of SBAF, with most of the data coming from the Australian dataset (133 granules versus 19 from the Amazon dataset). The spectra were sampled from the middle of the images, in the center of the swath. Although the spectra came from surface reflectance products, still some of them had to be manually removed as they showed traces of water vapor absorption (evidenced by plotting the spectra and observing the 940 nm band), were noisy, or did not report values. After filtering, the number of H0 spectra considered from each dataset was 54,333 from Australia, and 53,677 from the Amazon.

2.5. Relative spectral responses

Relative spectral responses (RSR) from AVHRR and TM5 were used to spectrally convolve the H0 surface reflectance spectra and derive spectral adjustment factors. Fig. 3 shows the RSR for each AVHRR sensor considered (N07 to N19), and for TM5. The RSR were obtained from <https://cloudsway2.larc.nasa.gov>.

2.6. MODIS land cover data

To analyze our results by land cover types we followed the International Geosphere-Biosphere Program (IGBP) classification included on

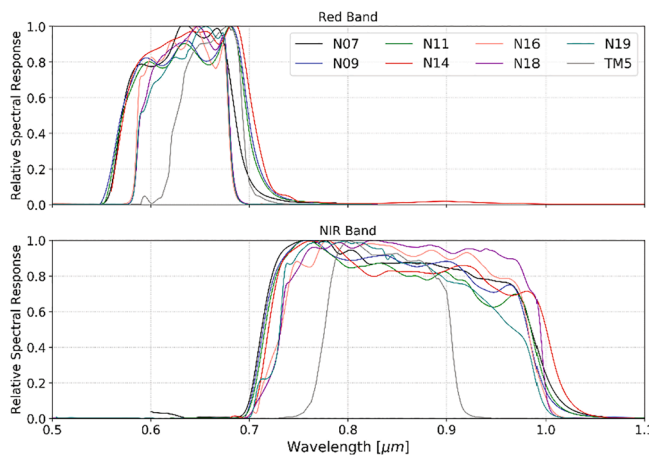


Fig. 3. AVHRR and Landsat5-TM Relative Spectral Responses.

the MODIS MCD12C1 product (Strahler et al., 1999). The MCD12C1 product provides yearly global land cover information in the CMG grid from 2001 to present year. To reduce possible misclassifications on years before the MODIS era, we generated a single classification map from all available years by selecting only the pixels that remained constant during the complete period. The original IGBP classes were then simplified following an approach similar to (Pérez-Hoyos et al., 2012).

Water areas were excluded from the analysis, and urban, snow, and wetland classes were removed because they had low pixel counts or were not present at all. The class reclassification scheme is showed in Table 1, and the global distribution of classes is shown in Fig. 4.

3. Methods

3.1. Selection of reference Landsat-5 TM dataset

The Landsat-5 scenes used as reference for this study were selected with the objective of maintaining a high spatial and temporal representativeness. This was achieved in two steps: First, we generated a global 5° latitude-longitude uniform grid of points and selected all Landsat-5 scenes that intersected a point for the complete period of study. Second, for the first and last year of each POES satellite, we selected all globally available scenes. In both cases, we discarded the scenes that had more than 60% of cloud cover over land. This process generated a database of more than 740,000 globally distributed scenes (Figs. 1 and 2). Finally, for all remaining scenes we downloaded a 120kmx120km subset located at the center of each image. Scene selection, sub-setting, and download was done through Google Earth Engine's API for python. Due to the large number of scenes, we parallelized any further processing using GNU Parallel (Tange, 2011).

3.2. Spatial aggregation of Landsat 5 TM surface reflectance

The first step in the evaluation was to aggregate the 30 m TM5 surface reflectance pixels to the scale of the AVHRR climate modeling grid (CMG) of 0.05°x0.05°. For this, we first selected the valid TM5 pixels following the criteria proposed by (Claverie et al., 2015): clear land pixels (with no cloud, cloud-shadow, water, or snow), that show no saturation, and with an atmospheric opacity lower than 0.3 (clear: < 0.1; average: 0.1 > 0.3; cloudy: > 0.3). Once the valid pixels were selected, we aggregated them to CMG scale using an averaging filter. Finally, we discarded all aggregated pixels generated from less than 100% valid TM5 pixels.

3.3. Geometric adjustment of AVHRR surface reflectance

The AVHRR LTDR product is originally normalized to a sun zenith angle (θ_s) of 45°; view zenith angle (θ_v) of 0°; and relative azimuth angle (φ) of 0°. To analyze the impact of BRDF on the LTDR performance, we started by undoing the current normalization in order to have a baseline dataset with no geometric or spectral adjustment whatsoever. We refer to this dataset as “No adjustment” in the rest of the manuscript. It is important to remark that comparing reflectance data from different sensors without accounting for BRDF effects should be avoided, as different geometric configurations can produce different errors that depend on both sensors sun-view geometries and on the observed surface characteristics.

We then used the VJB method (Vermote et al., 2009) to account for observation geometry differences between AVHRR and Landsat-5, and

Table 1
Reclassification of IGBP land cover classes.

Abbreviation	New Class Name	Original IGBP Classes
NLF	Needleleaf Forest	Evergreen Needleleaf Forest, Deciduous Needleleaf Forest
BLF	Broadleaf Forest	Evergreen Broadleaf Forest, Deciduous Broadleaf Forest
SSM	Shrublands, Savannas, Mixed Forest	Open Shrubland, Closed Shrubland, Savannas, Woody Savannas, Mixed Forest
CGL	Croplands and Grasslands	Croplands, Grasslands, Cropland Natural Vegetation Mosaic
BRN	Bare Areas	Barren

adjust the AVHRR surface reflectance to the corresponding Landsat-5 sun and view angles. The surface reflectance (ρ) for a certain geometric configuration (Θ) can be expressed as:

$$\rho(\Theta) = k_{iso} + k_{vol}F_{vol}(\Theta) + k_{geo}F_{geo}(\Theta) \quad (1)$$

where Θ represents the observation conditions of solar zenith angle (θ_s), view zenith angle (θ_v), and relative azimuth angle between sun and sensor (φ); F_{geo} and F_{vol} are the geometric and volumetric scattering components that characterize the shape of the bidirectional reflectance distribution function (BRDF) (Maignan et al., 2004; Roujean et al., 1992); and k_{iso} , k_{vol} , and k_{geo} are isotropic, volumetric, and geometric kernels. It is possible to rewrite the model using variables $V = \frac{k_{vol}}{k_{iso}}$ and $R = \frac{k_{geo}}{k_{iso}}$ proposed by (Vermote et al., 2009):

$$\rho(\Theta) = k_{iso}(1 + VF_{vol}(\Theta) + RF_{geo}(\Theta)) \quad (2)$$

Both V and R can be derived as a function of the Normalized Difference Vegetation Index (NDVI) (Franch et al., 2014b; Vermote et al., 2009). If we assume no change in the surface between two observations (A , B) with different geometric configurations, we can express this relationship as:

$$\rho(\Theta_B) = \rho(\Theta_A) \frac{(1 + VF_{vol}(\Theta_B) + RF_{geo}(\Theta_B))}{(1 + VF_{vol}(\Theta_A) + RF_{geo}(\Theta_A))} \quad (3)$$

Following this relationship, we adjusted the same-day AVHRR surface reflectance to the corresponding TM5 observation geometry as:

$$\rho_{AVHRR}(\Theta_{TM5}) = \rho_{AVHRR}(\Theta_{AVHRR}) \frac{(1 + VF_{vol}(\Theta_{TM5}) + RF_{geo}(\Theta_{TM5}))}{(1 + VF_{vol}(\Theta_{AVHRR}) + RF_{geo}(\Theta_{AVHRR}))} \quad (4)$$

For this study, the AVHRR angles were obtained from the LTDR product, and the TM5 angles were computed as described in Section 2.3. The V and R parameters were obtained from a global database generated by (Vermote et al., 2009) from MODIS data. The matter of whether to use VJB parameters derived from MODIS or from AVHRR to normalize the BRDF effects of AVHRR surface reflectance was analyzed by (Villaescusa-Nadal et al., 2019b), who found that VJB parameters derived from MODIS performed 3% (Red) to 5% (NIR) better than ones derived from AVHRR itself.

3.4. Spectral adjustment of AVHRR surface reflectance

Relative spectral responses (RSR) determine how a continuous spectrum from the surface is recorded on a sensor discrete band. Thus, differences in RSR between AVHRR and TM5 can affect the results of the cross-comparison, and a spectral adjustment should be applied to mitigate this (Chander et al., 2013). Amongst spectral adjustment methods the statistical based ones are the most common (Villaescusa-Nadal et al., 2019a). These methods consist in deriving statistical relationships between two analogous bands using radiative transfer simulations (Li et al., 2014; Van Leeuwen et al., 2006), remotely sensed data (Li et al., 2014; Skakun et al., 2018), or hyperspectral spectra convolutions (Doelling et al., 2012; Miura et al., 2006). For this study, we derived the spectral adjustment factors using the latter method. We first extracted over 100,000 H0 atmospherically corrected reflectance spectra from two available datasets (more information is given in Section 2.4). Because the spectral mixture inside an AVHRR CMG pixel (~5600 m) is typically more diverse than that of a Hyperion pixel (30 m), we followed the approach proposed by (Villaescusa-Nadal et al., 2019a), and simulated a dataset of 500,000 surface reflectance spectra from the linear combination of up to three independent H0 spectra. This provided a spectra database more representative of the CMG pixels scale.

The generated spectra were convolved with each sensor RSR as shown in Eq. (5), where λ represents the Red or NIR band.

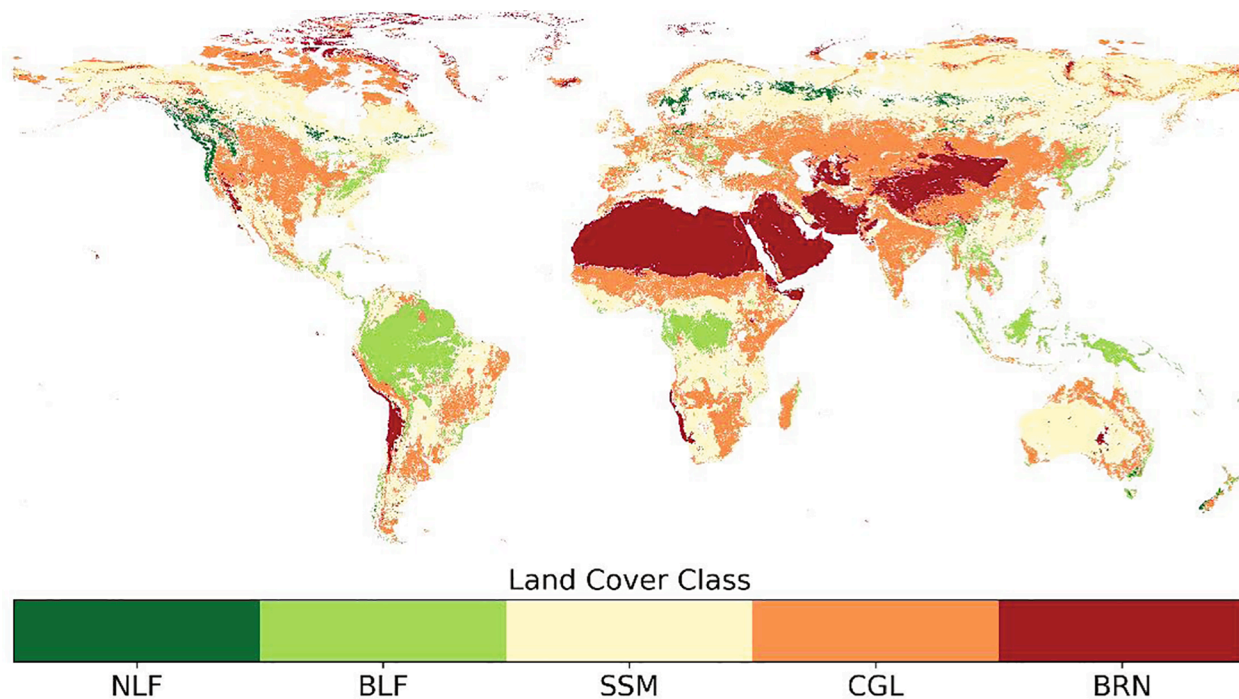


Fig. 4. International Geosphere-Biosphere Program (IGBP) land cover classification from MCD12C1 product. Labels were simplified according to Table 1.

$$\bar{\rho}_\lambda = \frac{\int \rho_\lambda RSR_\lambda d_\lambda}{\int RSR_\lambda d_\lambda} \quad (5)$$

The convolved values were used to derive spectral band adjustment factors (SBAF) for each TM5/AVHRR pair as:

$$SBAF_\lambda = \frac{\bar{\rho}_{\lambda, TM5}}{\bar{\rho}_{\lambda, AVHRR}} \quad (6)$$

We then tested several spectral adjustment models (Villaescusa-Nadal et al., 2019a) and found that the best fit was obtained by fitting the SBAFs to the quadratic NDVI:

$$SBAF_\lambda = a_\lambda + b_\lambda * NDVI_{AVHRR} + c_\lambda * NDVI_{AVHRR}^2 \quad (7)$$

Finally, we used the derived coefficients to spectrally adjust the AVHRR to TM5-like values.

$$\rho_{\lambda, TM5} = \rho_{\lambda, AVHRR} * SBAF_\lambda \quad (8)$$

3.5. Evaluation of surface reflectance

For the evaluation we assumed no daily variation of the surfaces and relied on same day AVHRR and TM5 acquisitions. We only considered AVHRR observations with a sun zenith angle smaller than 75° and view zenith angle smaller than 45°. Finally, we used the Local Outlier Factor method to remove any remaining outliers (Breunig et al., 2000). We evaluate the differences between AVHRR and TM5 using three statistical metrics designed to quantify the accuracy, precision, and uncertainty (APU).

The accuracy (A) represents the mean bias of the estimates versus the reference (ϵ_i):

$$Accuracy (A) = \frac{\sum_{i=1}^n \epsilon_i}{N} \quad (9)$$

The precision (P) represents the repeatability of the estimates corrected for the mean bias:

$$Precision (P) = \sqrt{\frac{1}{n-1} \sum_{i=1}^n (\epsilon_i - A)^2} \quad (10)$$

The uncertainty (U) represents the actual statistical deviation including the mean bias:

$$Uncertainty (U) = \sqrt{\frac{1}{n} \sum_{i=1}^n \epsilon_i^2} \quad (11)$$

To provide a better perspective of each band performance, it is helpful to show the uncertainty relative to the average reference value (m). The relative uncertainty (rU) is then computed as:

$$Relative\ Uncertainty (rU) = \frac{U}{m} \quad (12)$$

In this paper, we refer to the notion of A, P, and U defined in (Vermote and Kotchenova, 2008). Thus, higher values of A, P, and U reflect higher discrepancies between both datasets and lower values reflect a better agreement.

To assess the evaluation results, we compare the uncertainty values against a certain specification (S). For surface reflectance products this specification is based on a sensitivity analysis of the atmospheric correction method, which for both AVHRR LTDR and TM-5 LEDAPS is based on the 6S model and has been previously found to be $0.05\rho + 0.005$ (where ρ is the surface reflectance magnitude) (Vermote and Kotchenova, 2008; Vermote and Saleous, 2006b). Because in this study we evaluate AVHRR using TM-5 as a reference, the evaluation specification is then defined as the quadratic sum of each sensor's specification, which for this case is $0.071\rho + 0.0071$. This approach has been adopted by other surface reflectance evaluation and intercomparison studies (Claverie et al., 2015; Skakun et al., 2018).

4. Results

In this section we present the results from the AVHRR evaluation. First, we show the impact of the BRDF and spectral adjustment on the comparison between AVHRR and TM5 surface reflectance (Section 4.1); we then show the evaluation results in terms of the surface reflectance magnitude (Section 4.2), temporal evolution (Section 4.3), spatial distribution (Section 4.4), seasonal variation (Section 4.5), and land cover (Section 4.6). Finally we show the relationship between the Red and NIR

bands relative errors (Section 4.7).

4.1. Impact of geometric and spectral adjustment

We first analyzed the impact of the geometric and spectral adjustment on the accuracy, precision, and uncertainty. Fig. 5 shows the comparison between AVHRR and TM5 surface reflectance for four adjustment levels: No Adjustment, only BRDF adjustment, only spectral adjustment, and both BRDF and spectral adjustments.

The BRDF adjustment improved the results of all metrics for both bands. In particular, the improvements were more evident on the Precision metric, which represents the scattering of the errors between AVHRR and TM5 and is mainly affected by differences in their sun-view geometry. The accuracy metric also showed improvements with BRDF correction but were not as consistent across all sensors. When the spectral adjustment was applied to the not-BRDF adjusted data, the results tended to show worse agreement between AVHRR and TM5, with only minor improvements in the best of cases. In general, the best results for accuracy, precision and uncertainty were achieved when both adjustments were applied to the AVHRR data.

For all cases, the Red band showed lower uncertainty values than the NIR. However, because the surface reflectance magnitudes on the NIR are usually higher, its relative uncertainties were lower. Table 2 summarizes the relative uncertainty results for the case with no adjustment and with both BRDF and spectral adjustments.

4.2. Performance of LTDR in terms of reflectance magnitude

Performance of surface reflectance products varies with the reflectance magnitude of the measured target. Here we present this dependence using APU graphs (Vermette and Kotchenova, 2008), which represent the accuracy, precision, and uncertainty for a range of reference reflectance values. Fig. 6 shows APU graphs of the evaluation for each sensor and band using both the geometric and spectral adjustments. For most sensor-band combinations, the uncertainty increased with surface reflectance magnitude but remained under the combined specification ($0.071\rho + 0.0071$). For the Red band, average values ranged between -0.001 to 0.005 for the accuracy, 0.012 to 0.019 for the precision, and 0.014 to 0.020 for the uncertainty. In the case of the NIR band, the average values ranged between -0.008 and 0.014 for the accuracy, 0.019 to 0.027 for the precision, and 0.020 to 0.028 for the uncertainty. Overall, data from KLM (N16 to N19) sensors showed better performance than pre-KLM ones (N07 to N14).

4.3. Temporal evolution of LTDR performance

Performance of a satellite data record can change in time, as changes

Table 2

Relative uncertainty before adjustment and after BRDF and spectral adjustment.

Band/Adjustment	N07	N09	N11	N14	N16	N18	N19
Red/No Adjustment	23%	22%	19%	18%	18%	17%	17%
Red/BRDF + Spectral	14%	13%	11%	11%	10%	12%	13%
NIR/No Adjustment	20%	21%	17%	20%	17%	16%	14%
NIR/BRDF + Spectral	10%	10%	9%	10%	9%	10%	8%

in platform orbit, sensor degradation, and data calibration can affect the quality of top-of-atmosphere data. Moreover, performance of the atmospheric correction process depends on the quality of available ancillary data used to characterize atmospheric conditions. In this regard, it is important to evaluate how the performance of the AVHRR LTDR changes with time. Fig. 7 shows the temporal evolution of the APU metrics during the 1984–2011 study period. Yearly results are shown for each sensor-band combination for the geometrical and spectrally adjusted AVHRR data. Accuracies showed a generally consistent behavior for each independent sensor, i.e., in most cases a particular AVHRR sensor showed either negative or positive bias with respect to TM5. One exception was N11 NIR band, which exhibited variations in the bias direction during its lifetime and an opposite bias behavior both when transitioning from its predecessor (N11) and to its successor (N14). In terms of precision, the pre-KLM sensors (N07–N014) showed an increasing trend of the P metric during their lifetimes that was present in both bands. This was not the case for the KLM sensors (N16–N19) which showed a more stable temporal behavior.

4.4. Spatial distribution of bias and relative uncertainty

Performance of the LTDR is not spatially uniform. Two metrics helpful to represent this are the accuracy, which shows the mean bias of AVHRR with respect to TM5; and the relative uncertainty, which gives context to the uncertainty metric in relation to the actual average reflectance of a particular site. We display these metrics in 2.5° latitude and longitude bins that provide enough data to compute the statistical metrics. For each bin, the metrics were computed from all included CMG pixels. Wider spatial coverage in the results of newer AVHRR sensors is due to a larger number of TM5 scenes available and is not related with AVHRR data availability.

Accuracy results showed lower biases for the Red than for the NIR band (Fig. 8). The Red band accuracy values for 95% of bins varied within -0.028 to 0.026 for N07, -0.015 to 0.018 for N09, -0.021 to 0.013 for N11, -0.012 to 0.014 for N14, -0.008 to 0.012 for N16, -0.005 to 0.015 for N18, and -0.003 to 0.015 for N19. For the NIR band, accuracy values for 95% of the bins varied within -0.040 to 0.017 for N07, -0.025 to 0.025 for N09, -0.026 to 0.014 for N11, -0.008 to 0.034 for N14, -0.008 to 0.023 for N16, -0.006 to 0.022 for N18, and

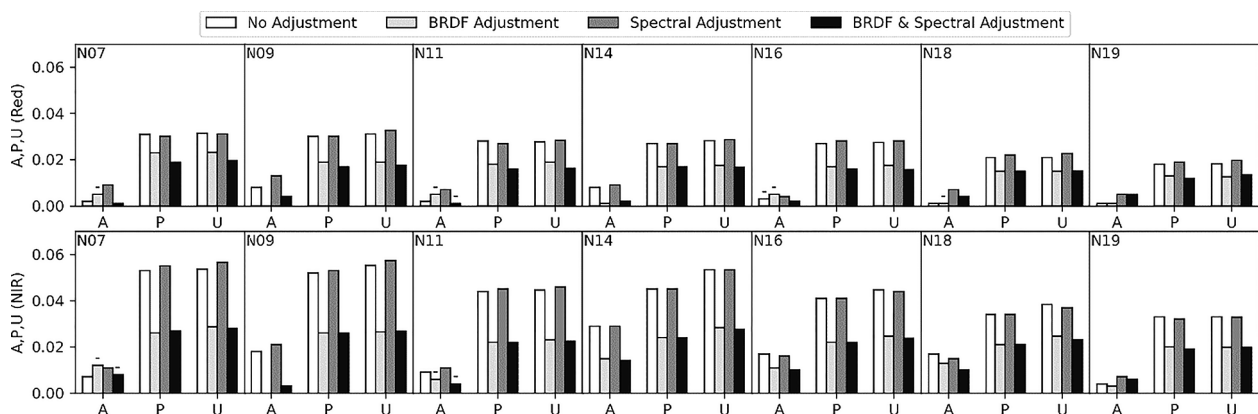


Fig. 5. Impact of the geometrical and spectral adjustments on the accuracy (A), precision (P), and uncertainty (U). Results are shown for the Red (top row) and NIR (bottom row) bands. A “-” sign above the accuracy bars indicates negative values. Lower values show better agreement between AVHRR and Landsat-5 TM.

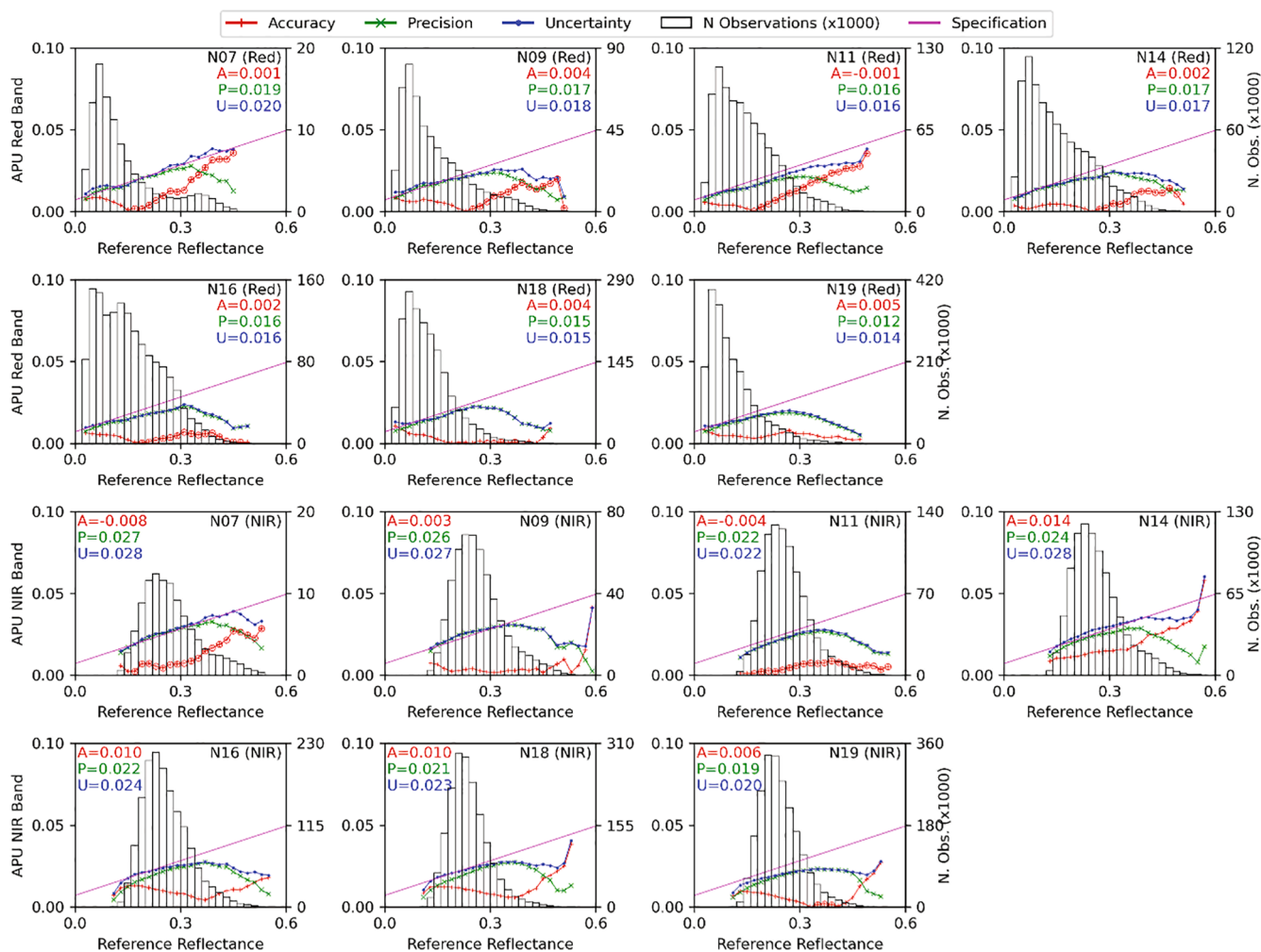


Fig. 6. Accuracy (A), Precision (P), and Uncertainty (U) of AVHRR surface reflectance evaluation. Metrics are computed on bins of 0.02 reflectance units and the overall value is given in the top of each subplot. The histogram of values is displayed in black (right axis). Circles on the accuracy line represent negative values. The magenta line represents the specification of $0.071\rho + 0.0071$ from the TM5 product. (For interpretation of the references to colour in this figure legend, the reader is referred to the web version of this article.)

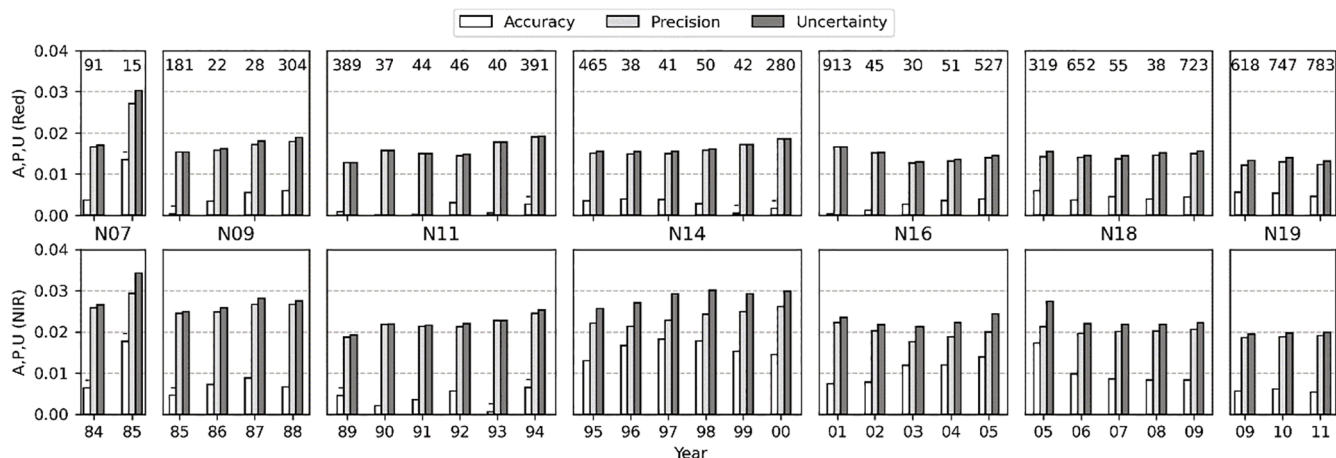


Fig. 7. Temporal evolution of the Accuracy, Precision, and Uncertainty. A “-” sign above the accuracy bar represents negative values. The number of CMG pixels (in thousands) is shown at the top.

-0.001 to 0.018 for N19. There is a change in the bias direction and magnitude (sign of the accuracy value) on the NIR band when transitioning from N11 to N14 which is especially noticeable on Northern

Africa and Western Asia.

The spatial distribution of relative uncertainties was generally consistent between all sensors (Fig. 9). The highest relative uncertainties

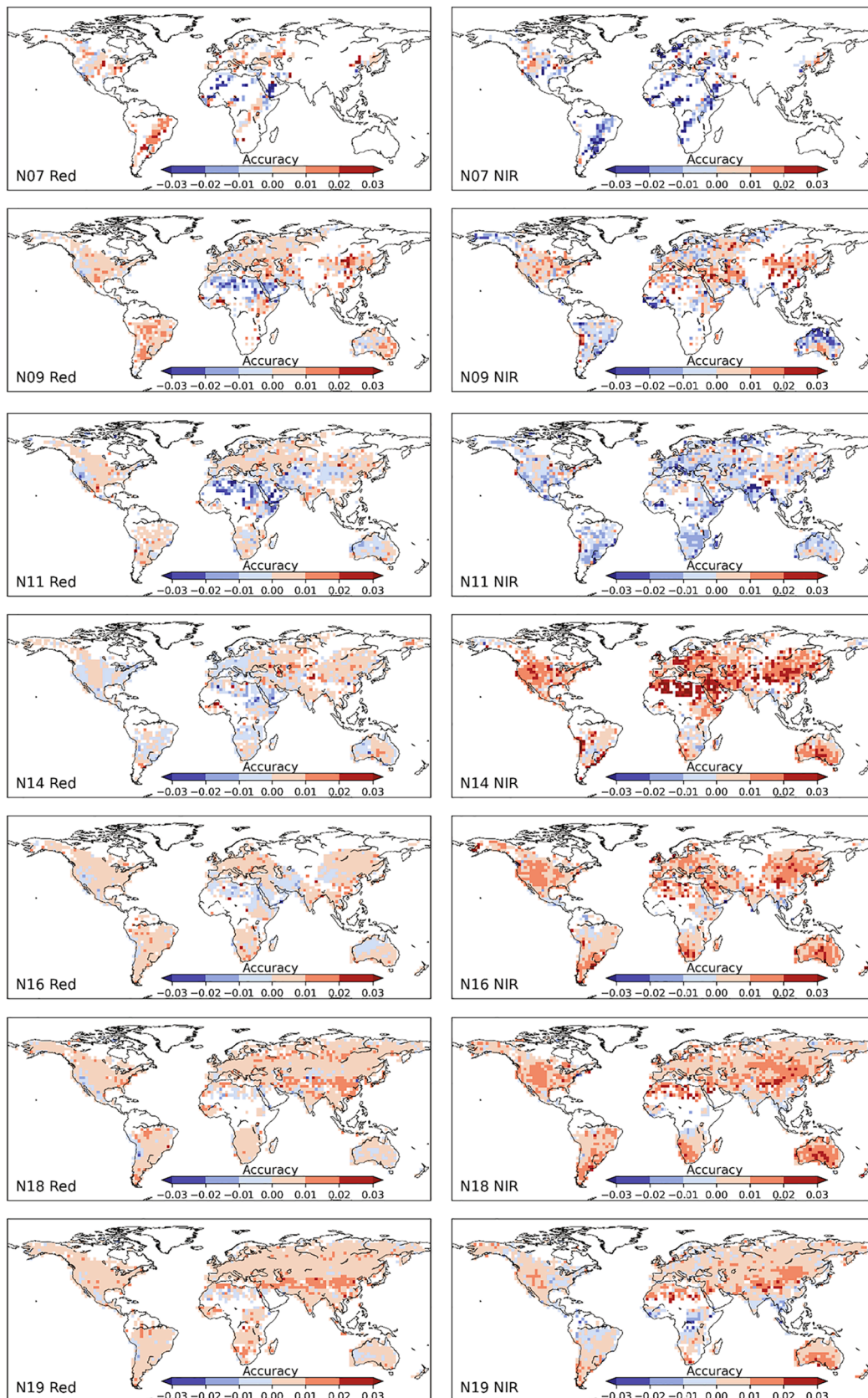


Fig. 8. Accuracy maps for AVHRR LTDR Red and NIR bands. Values closer to 0 represent better performance. The values were computed in 2.5° (latitude and longitude) bins considering all corresponding CMG pixels. (For interpretation of the references to colour in this figure legend, the reader is referred to the web version of this article.)

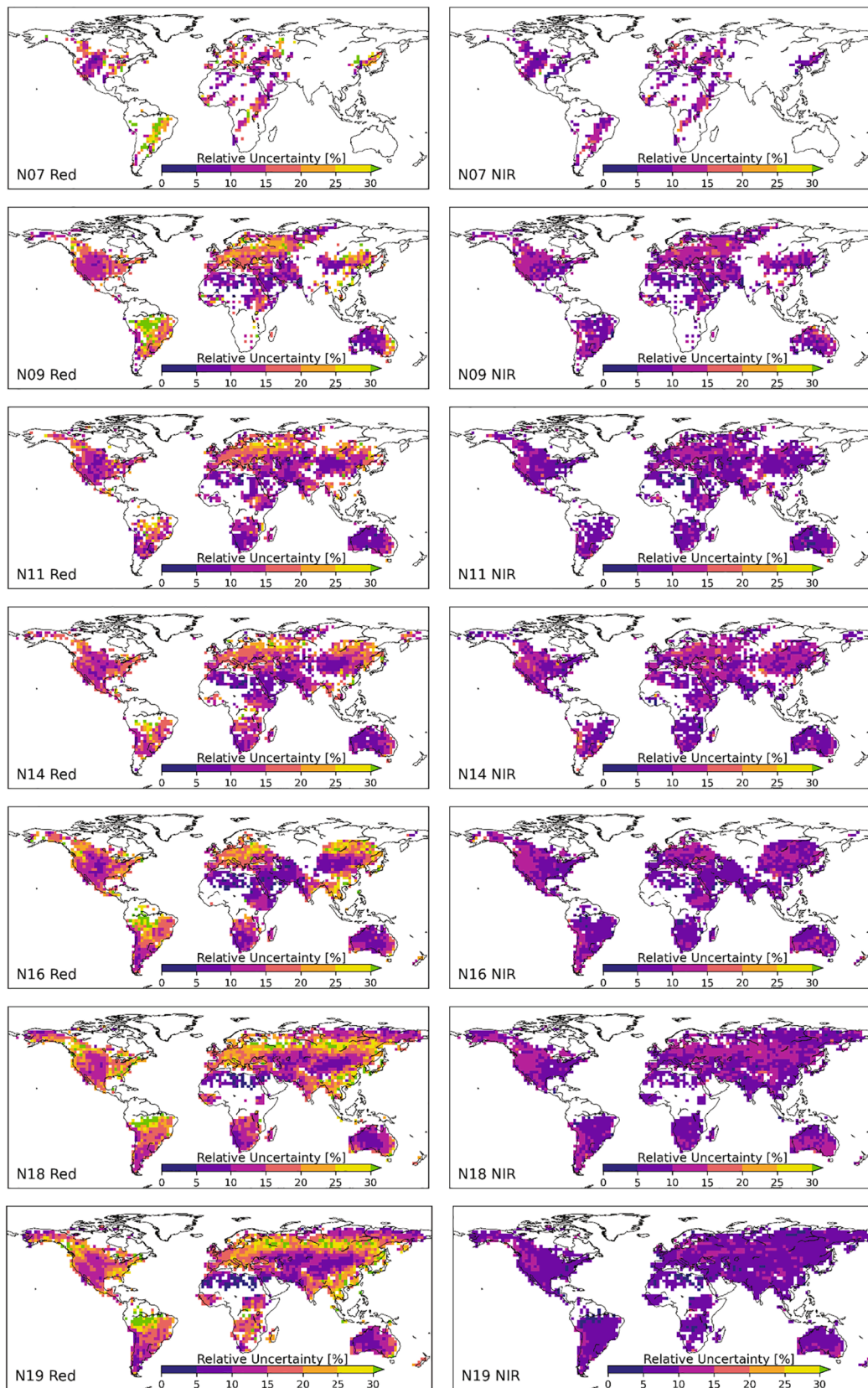


Fig. 9. Relative uncertainty maps for AVHRR LTDR Red and NIR bands. Values closer to 0 represent better performance. The values were computed in 2.5° (latitude and longitude) bins considering all corresponding CMG pixels. (For interpretation of the references to colour in this figure legend, the reader is referred to the web version of this article.)

were observed over high latitudes and over tropical regions. In particular, the largest values were observed over the Amazon forest, where the density of observation is low due to frequent cloud cover. The Red band showed worse performance than the NIR. When considering 95% of the bins, the global relative uncertainty average values for the Red band were (15 ± 6)% for N07, (14 ± 6)% for N09, (13 ± 4)% for N11, (13 ± 4)% for N14, (14 ± 6)% for N16, (16 ± 6)% for N18, and (15 ± 6)% for N19. In the NIR band, the values were (10 ± 3)% for N07, (10 ± 2)% for N09, (9 ± 2)% for N11, (10 ± 2)% for N14, (9 ± 2)% for N16, (9 ± 2)% for N18, and (8 ± 2)% for N19. On the next sections, we analyze these results in terms of seasonality and land cover class.

4.5. Seasonal variation of LTDR bias and relative uncertainty

The seasonal variation of the Accuracy and Relative Uncertainty are shown in Fig. 10. The metrics were first computed per pixel, and then aggregated by season and analyzed for the Northern (NH) and Southern (SH) hemispheres separately. Seasons correspond to December-January-February (DJF), March-April-May (MAM), June-July-August (JJA), and September-October-November (SON). Only pixels with more than 30 valid observations were considered in the analysis. The number of pixels per season, hemisphere, and satellite is shown in Table 3.

The number of pixels with more than 30 observations is, in average, around 4 times larger on the Northern hemisphere than in the Southern hemisphere, which is likely due to distribution of land bodies as well as TM5 data availability. On both hemispheres, the JJA season showed the highest number of observations available.

Average Red band accuracies ranged between -0.013 ± 0.015 (N07 in DJF) to 0.007 ± 0.006 (N18 in JJA) on the northern hemisphere, and

between -0.024 ± 0.017 (N07 in MAM) to 0.019 ± 0.009 (N07 in JJA) on the southern hemisphere. Results for the NIR band showed average accuracies that ranged between -0.021 ± 0.014 (N07 in DJF) to 0.015 ± 0.012 (N14 in JJA) on the northern hemisphere, and between -0.024 ± 0.017 (N07 in MAM) to 0.019 ± 0.009 (N07 in JJA) on the southern hemisphere. For most cases, the spread of values was generally similar between the Red and NIR bands. In terms of relative uncertainties, average values for the Red band ranged between (10 ± 5)% (N16 in DJF) to (20 ± 8)% (N18 in JJA) on the northern hemisphere, and between (10 ± 5)% (N11 in JJA) to (37 ± 13)% (N07 in MAM) in the southern hemisphere. In the case of the NIR band, average values ranged between (8 ± 2)% (N19 in DJF) to (11 ± 4)% (N07 in DJF) on the northern hemisphere, and between (7 ± 2)% (N11 in JJA) to (13 ± 6)% (N07 in MAM) in the southern hemisphere.

4.6. Accuracy and relative uncertainty analysis by land cover

Accuracy and relative uncertainty aggregated by land cover class are shown in Fig. 11. The land cover classes analyzed correspond to the ones shown in Table 1. The metrics were first computed per pixel, and then aggregated by land cover class. Only pixels with more than 30 valid observations were considered for the analysis. The number of pixels per land cover class for each POES satellite is shown in Table 4.

Average accuracy values for the Red and NIR bands showed little variation between sensors and land cover classes. Values ranged between -0.016 ± 0.013 (N07 on BRN) to 0.012 ± 0.005 (N18 on NLF) for the Red band, and between -0.014 ± 0.015 (N07 on BRN) to 0.02 ± 0.019 (N14 on NLF) for the NIR band. The newer sensors generally showed less variability within the same land cover. Overall, the largest

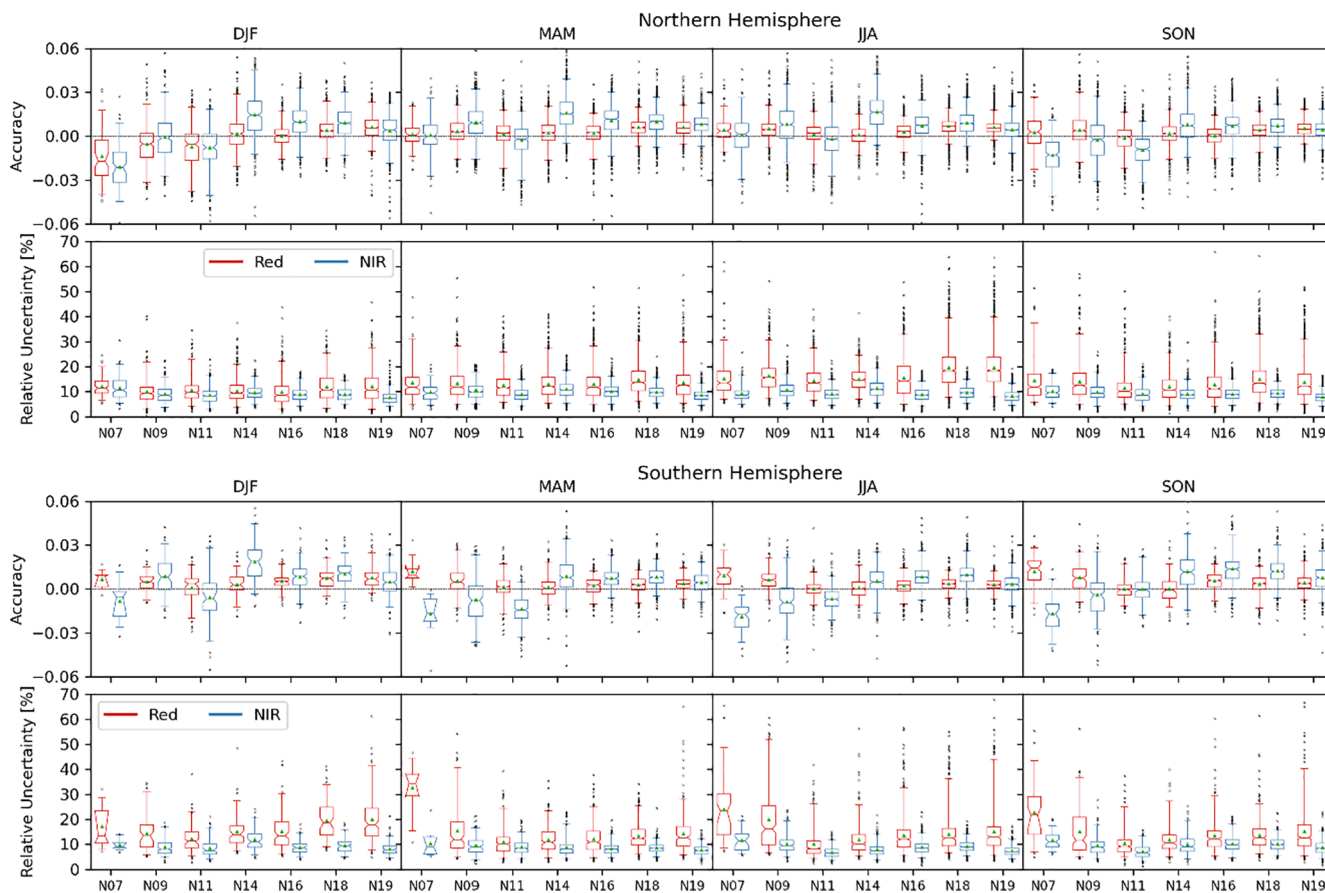


Fig. 10. Seasonal variation of accuracy and relative uncertainty for Red and NIR bands on the northern (top) and southern (bottom) hemispheres. Boxplot notches represent the median confidence interval. Green triangles represent the mean. Values outside the 2.5th and 97.5th percentiles are plotted individually outside the boxplot whiskers. (For interpretation of the references to colour in this figure legend, the reader is referred to the web version of this article.)

Table 3
Number of CMG pixels per season.

Platform	Season							
	Northern Hemisphere				Southern Hemisphere			
	DJF	MAM	JJA	SON	DJF	MAM	JJA	SON
N07	14,527	14,109	27,725	19,077	1,695	862	7,152	4,631
N09	50,760	98,427	114,798	97,697	13,442	20,172	32,442	21,383
N11	66,669	179,228	219,928	147,291	17,795	50,791	96,986	28,075
N14	123,343	166,604	146,475	182,020	10,230	42,750	82,012	29,062
N16	142,899	258,199	323,567	255,178	32,492	63,199	175,859	62,986
N18	95,938	171,564	282,999	415,161	16,426	118,936	300,556	94,323
N19	129,799	201,134	522,381	494,477	24,814	109,541	184,704	100,931

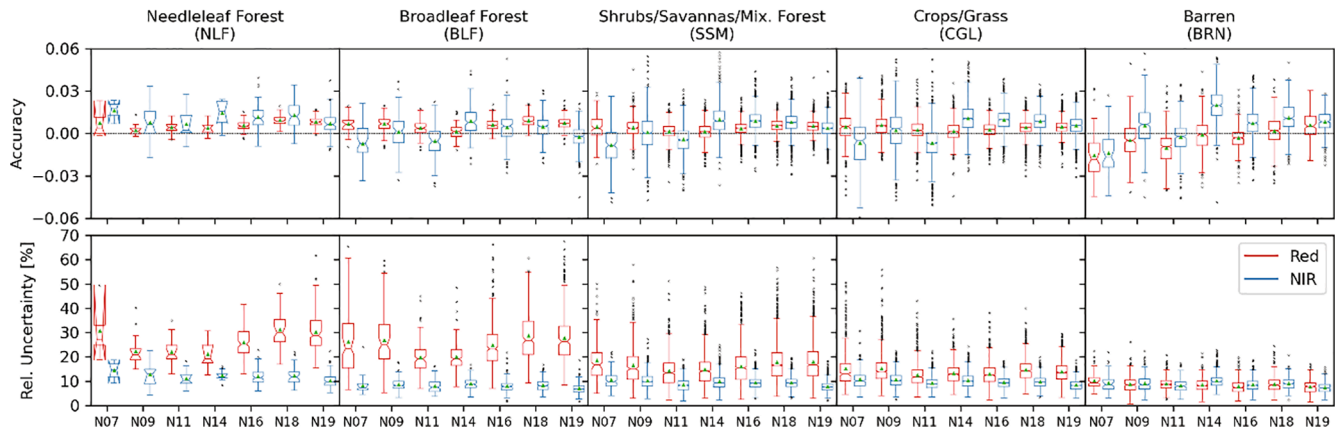


Fig. 11. Accuracy (top) and relative uncertainty (bottom) results by land cover class for Red and NIR bands. Boxplot notches represent the median confidence interval. Green triangles represent the mean. Values outside the 2.5th and 97.5th percentiles are plotted individually outside the boxplot whiskers. (For interpretation of the references to colour in this figure legend, the reader is referred to the web version of this article.)

Table 4
Number of CMG pixels per land cover class.

Platform	Land Cover Class				
	NLF	BLF	SSM	CGL	BRN
N07	435	4,674	18,985	50,202	15,548
N09	2,770	17,543	120,336	225,264	82,994
N11	2,855	17,168	204,620	422,263	159,665
N14	1,951	16,295	189,696	368,736	205,684
N16	12,485	42,271	372,754	565,779	320,876
N18	11,090	44,301	557,509	755,103	127,602
N19	21,853	82,534	649,113	850,797	162,205

spread of values was shown by the BRN class. In terms of relative uncertainties, results showed that for the Red band the largest uncertainties occurred on the Forest classes, which ranged between $(19 \pm 9)\%$ (N14 on BLF) to $(34 \pm 14)\%$ (N18 on NLF). In contrast, the BRN class showed the lowest relative uncertainties, ranging between $(8 \pm 3)\%$ (N16) to $(10 \pm 4)\%$ (N18). In the case of the NIR band, results were more consistent between land classes and sensors, and were noticeably lower than those of the Red band, ranging between $(7 \pm 2)\%$ (N19 on BLF) to $(14 \pm 8)\%$ (N14 on NLF).

4.7. Relationship between Red and NIR bands relative errors

Knowledge of possible correlation between the Red and NIR band errors can be of interest for downstream data producers and users. In this context, Fig. 12 shows the spatial distribution of the determination coefficient (R2) computed between the Red and NIR bands relative errors with data from all AVHRR sensors. Results showed a strong relationship between relative errors over bare areas in North Africa and Southern Asia (R2 greater than 0.8), and over open shrubland areas in North

America, South America, South Africa, and Australia (R2 greater than 0.5). Similar results were obtained for each sensor independently but are excluded for brevity.

5. Discussion

In this paper, we evaluated the performance of the AVHRR surface reflectance long-term data record between 1984 and 2011 using Landsat-5 TM surface reflectance as reference. While the current LTDR temporal coverage spans the period between 1982 to present day, we limited this study to the period where Landsat-5 was active. This allowed us to evaluate the performance of all AVHRR sensors with one consistent reference that has gone through a series of strict recalibration procedures (Chander et al., 2009).

The VJB method was used to normalize the AVHRR surface reflectance to the observation geometry of TM5, which largely improved the uncertainties between sensors, and is explained by the diminution of errors generated from the very different observation geometries. These results agree with previous studies (Bréon and Vermote, 2012; Franch et al., 2014a, 2019; Villaescusa-Nadal et al., 2019b) that showed the good performance of the BRDF-adjustment obtained with the VJB method. In this paper, we used global V and R coefficients derived from MODIS and applied them to adjust AVHRR data, which are the same coefficients used to normalize the BRDF in the LTDR product.

Adjustment of spectral differences showed mixed performance. When applied alone, only a couple of sensor-band combinations improved the agreement between AVHRR and TM5, and the general results showed an overcompensation and increase of bias. On the other hand, when the SBAFs were used to spectrally adjust the BRDF-normalized data, results improved as it further reduced the mean bias between AVHRR and TM5 for almost all cases. This might be explained by the dependence of the spectral adjustment factors on the NDVI, which

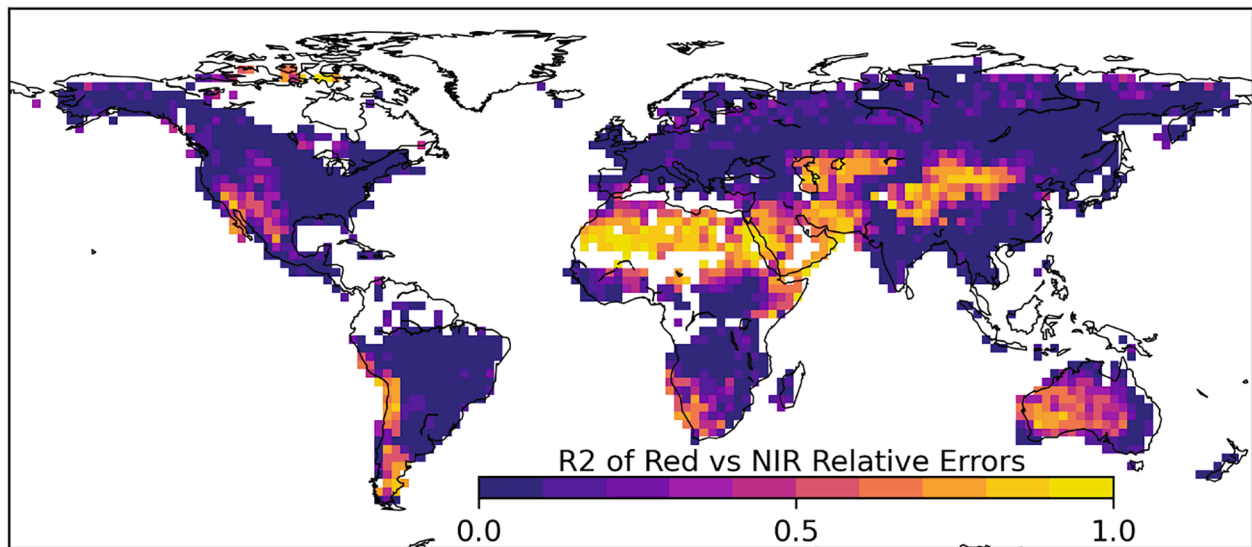


Fig. 12. Determination coefficient between Red and NIR bands relative errors. The values were computed in 2.5° (latitude and longitude) bins considering all corresponding CMG pixels. (For interpretation of the references to colour in this figure legend, the reader is referred to the web version of this article.)

although is less perturbed than independent bands to observation geometry, it is affected to some extent due to the increase of BRDF effects with wavelength, something that is evidenced by the larger improvements on the NIR band after the BRDF adjustment showed in Fig. 5, and that is in agreement with previous studies (Brown De Colstoun and Walthall, 2006; Claverie et al., 2015; Mahtab et al., 2009). The largest improvements in APU were obtained with both the BRDF and spectral adjustments applied.

The accuracy, precision, and uncertainty (APU) graphs revealed similar performance between the Red and NIR bands, with results for most of the AVHRR sensor-bands close or within the combined AVHRR and TM5 specification. Regarding the shape of the APU curves, two effects can be noted: First, the aerosol and Rayleigh scattering that increase the signal reaching the sensor at low surface reflectance values; and second, the signal attenuation by aerosol absorption that occurs at higher values (Kaufman, 1987). These effects are shown by the APU with low and high reflectance values showing a positive and negative bias, respectively.

Temporal variations in APU were relatively small, with a general decreasing trend during the study period. In the case of the N07-N14, there is an increase in the uncertainty during the lifetime of each sensor, which can be attributed to their orbital drift (Kaufmann et al., 2000; Latifovic et al., 2012). This effect was not evident on N16-N19 platforms, as their orbits were more stable during the years included in the study period. These results were consistent with the errors reported by the previous evaluation of N16-N19 surface reflectance using MODIS (Franch et al., 2017). Seasonal analysis of relative uncertainties did not show significant differences between seasons.

The spatial distribution of accuracies showed better performance of the Red band, which had biases closer to zero and that were more stable. Results for the NIR showed inconsistencies in the biases between some sensors, which were more noticeable between N11 and N14. These results are coherent to findings of previous studies that reported abrupt changes in the LTDR surface reflectance magnitude when transitioning between sensors (Giglio and Roy, 2020; Song et al., 2018a, 2018b). Spatial distribution of relative uncertainties was consistent between the sensors on all POES satellites. The highest values were located over high latitudes and over tropical regions, which might be attributed to stronger atmospheric effects (Vermote and Kotchenova, 2008), cloud and snow pixel miss-classification in these areas (Claverie et al., 2015; Feng et al., 2013), and varying performance of the LTDR over different land cover types. The latter was also evidenced by the land cover analysis that

revealed larger and less consistent uncertainties over forest classes. Overall, the NIR showed lower relative uncertainties than the Red, which is due to the normally higher NIR reflectance magnitudes.

The spatial analysis of Red versus NIR bands errors showed strong correlations over barren and sparsely vegetated areas, which are commonly associated with low values of vegetation indices such as the Normalized Difference Vegetation Index (NDVI) and 2-band Enhanced Vegetation Index (EVI2). In contrast, only weak relationships were found over other regions and land covers. This might be of particular interest to producers and users of AVHRR land datasets, as error correlation between bands can impact downstream products.

6. Conclusions

In this study we evaluated the accuracy, precision, and uncertainty of the AVHRR Long Term Data Record for the period 1984–2011 using globally distributed data from the Thematic Mapper sensor onboard Landsat-5 used as a reference. The evaluation was carried out for the AVHRR sensor on each POES satellite independently.

We analyzed four different adjustment levels of AVHRR data: a “No-Adjustment” level, obtained by removing the BRDF normalization initially present on the LTDR product, which represents the original AVHRR data after the atmospheric correction process; a “BRDF adjusted level” which was obtained by implementing the VJB method to account for reflectance variations due to changes in sun and view geometries; a “spectrally adjusted level”, where spectral adjustment factors derived from Hyperion hyperspectral data were applied to minimize the band spectral differences between sensors; and a final adjustment stage, where both the BRDF and spectral adjustments are applied. The VJB BRDF-correction method used in the LTDR showed good performance when it was used to adjust the AVHRR observations to the Landsat-5 geometry, reducing the uncertainties when compared to unadjusted data. The spectral adjustment factors derived from Hyperion data proved to be efficient, when applied to BRDF-normalized data, further reducing the uncertainties in most cases. However, when it was applied to data without BRDF correction, the results were mixed, and evidence of over adjustment was observed.

Results of the cross-comparison showed a good agreement between AVHRR and TM5, with uncertainties that were close to or within the proposed combined specification of $0.071\rho + 0.0071$. The Red band showed biases closer to zero and more temporally consistent than the NIR band, which broad spectral response makes it especially sensitive to

water vapor absorption effects. Moreover, certain regions showed inconsistencies in the surface reflectance bias between contiguous AVHRR sensors, which suggests that, depending on the nature of their study, data users might still need to utilize data normalization steps and carefully examine their results for artifacts. Nevertheless, the LTDR is an ever-evolving project, and future versions will concentrate on mitigating these data inconsistencies which might arise from orbital drift, inter-satellite calibration issues, spectral differences, BRDF normalization, or quality of ancillary data products for atmospheric characterization. In this regard, we urge the users to always consult the most recent ATBD and user's guide available for better understanding of the current LTDR processing.

This work presents the first comprehensive evaluation of the AVHRR surface reflectance Long Term Data Record that encompasses data from the seven POES satellites, providing valuable information on its performance and uncertainties. Future research will focus on analyzing the uncertainty sources, and on improving the atmospheric correction of the LTDR through the retrieval of water vapor concentration from AVHRR data and the implementation of aerosol correction over land.

Funding

This research was funded by the National Aeronautics and Space Administration (NASA) grant number 80NSSC18M0063 and partially supported by the program Generacio Talent of Generalitat Valenciana (CIDEAGENT/2018/009).

Credit authorship contribution statement

Andres Santamaria-Artigas: Conceptualization, Methodology, Writing - original draft, Writing - review & editing. **Eric Vermote:** Conceptualization, Methodology, Writing - review & editing, Supervision. **Belen Franch:** Conceptualization, Methodology, Writing - review & editing, Supervision. **Jean-Claude Roger:** Conceptualization, Writing - review & editing, Supervision. **Sergii Skakun:** Methodology, Writing - review & editing, Supervision.

Declaration of Competing Interest

The authors declare that they have no known competing financial interests or personal relationships that could have appeared to influence the work reported in this paper.

References

- Bhatt, R., Doelling, D.R., Scarino, B.R., Gopalan, A., Haney, C.O., Minnis, P., Bedka, K.M., 2016. A Consistent AVHRR Visible Calibration Record Based on Multiple Methods Applicable for the NOAA Degrading Orbits. Part I: Methodology. *J. Atmos. Ocean. Technol.* 33, 2499–2515. <https://doi.org/10.1175/JTECH-D-16-0044.1>.
- Bréon, F.M., Vermote, E.F., 2012. Correction of MODIS surface reflectance time series for BRDF effects. *Remote Sens. Environ.* 125, 1–9. <https://doi.org/10.1016/j.rse.2012.06.025>.
- Breunig, M.M., Krieger, H.P., Ng, R.T., Sander, J., 2000. LOF: Identifying Density-Based Local Outliers, in: In: ACM SIGMOD International Conference on Management of Data. <https://doi.org/10.1093/acprof>.
- [dataset] Broomhall, M., 2012. AusCover/Curtin Hyperion Enhancement and Atmospheric Correction Technique ATBD. <http://www.auscover.org.au/purl/hyperspectral-surf-refl-hyperion>.
- Brown De Colstoun, E.C., Walthall, C.L., 2006. Improving global scale land cover classifications with multi-directional POLDER data and a decision tree classifier. *Remote Sens. Environ.* 100, 474–485. <https://doi.org/10.1016/j.rse.2005.11.003>.
- [dataset] Chambers, J.Q., 2012. LBA-ECO CD-34 Hyperion 30-m Surface Reflectance, Amazon Basin: 2002-2005. ORNL DAAC, Oak Ridge, Tennessee, USA. <https://doi.org/10.3334/ORNLDAAC/1064>.
- Chander, G., Helder, D.L., Markham, B.L., Dewald, J.D., Kaita, E., Thome, K.J., Micijevic, E., Ruggles, T.A., 2004. Landsat-5 TM Reflective-Band Absolute Radiometric Calibration. *IEEE Trans. Geosci. Remote Sens.* 42 <https://doi.org/10.1109/TGRS.2004.836388>.
- Chander, G., Markham, B., 2003. Revised Landsat-5 TM Radiometric Calibration Procedures and Postcalibration Dynamic Ranges. *IEEE Trans. Geosci. Remote Sens.* 41 <https://doi.org/10.1109/TGRS.2003.818464>.

- Chander, G., Markham, B.L., Helder, D.L., 2009. Summary of current radiometric calibration coefficients for Landsat MSS, TM, ETM+, and EO-1AL1 sensors. *Remote Sens. Environ.* 113, 1–24. <https://doi.org/10.1016/j.rse.2009.01.007>.
- Chander, G., Mishra, N., Helder, D.L., Aaron, D.B., Angal, A., Choi, T., Xiong, X., Doelling, D.R., 2013. Applications of spectral band adjustment factors (SBAF) for cross-calibration. *IEEE Trans. Geosci. Remote Sens.* 51, 1267–1281. <https://doi.org/10.1109/TGRS.2012.2228007>.
- Claverie, M., Matthews, J., Vermote, E.F., Justice, C.O., 2016. A 30+ Year AVHRR LAI and FAPAR Climate Data Record: Algorithm Description and Validation. *Remote Sens.* 8, 263. <https://doi.org/10.3390/rs8030263>.
- Claverie, M., Vermote, E.F., Franch, B., Masek, J.G., 2015. Evaluation of the Landsat-5 TM and Landsat-7 ETM + surface reflectance products. *Remote Sens. Environ.* 169, 390–403. <https://doi.org/10.1016/j.rse.2015.08.030>.
- Doelling, D.R., Lukashin, C., Minnis, P., Scarino, B., Morstad, D., 2012. Spectral reflectance corrections for satellite intercalibrations using SCIAMACHY data. *IEEE Geosci. Remote Sens. Lett.* 9, 119–123. <https://doi.org/10.1109/LGRS.2011.2161751>.
- Feng, M., Sexton, J.O., Huang, C., Masek, J.G., Vermote, E.F., Gao, F., Narasimhan, R., Channan, S., Wolfe, R.E., Townshend, J.R., 2013. Global surface reflectance products from Landsat: Assessment using coincident MODIS observations. *Remote Sens. Environ.* 134, 276–293. <https://doi.org/10.1016/j.rse.2013.02.031>.
- Franch, B., Vermote, E.F., Skakun, S., Roger, J.-C., Masek, J., Ju, J., Villaseca-Nadal, J. L., Santamaria-Artigas, A., 2019. A Method for Landsat and Sentinel 2 (HLS) BRDF Normalization. *Remote Sens.* 11 <https://doi.org/10.3390/rs11060632>.
- Franch, B., Vermote, E.F., Claverie, M., 2014a. Intercomparison of Landsat albedo retrieval techniques and evaluation against in situ measurements across the US SURFRAD network. *Remote Sens. Environ.* 152, 627–637. <https://doi.org/10.1016/j.rse.2014.07.019>.
- Franch, B., Vermote, E.F., Roger, J.C., Murphy, E., Becker-reshef, I., Justice, C., Claverie, M., Nagol, J., Csiszar, J., Meyer, D., Baret, F., Masuoka, E., Wolfe, R., Devadiga, S., 2017. A 30+ year AVHRR land surface reflectance climate data record and its application to wheat yield monitoring. *Remote Sens.* 9, 1–14. <https://doi.org/10.3390/rs9030296>.
- Franch, B., Vermote, E.F., Sobrino, J.A., Julien, Y., 2014b. Retrieval of surface albedo on a daily basis—application to MODIS data. *IEEE Trans. Geosci. Remote Sens.* 52ID–30, 7549–7558. <https://doi.org/10.1109/TGRS.2014.2313842>.
- Giglio, L., Roy, D.P., 2020. On the outstanding need for a long-term, multi-decadal, validated and quality assessed record of global burned area: Caution in the use of Advanced Very High Resolution Radiometer data. *Sci. Remote Sens.* 2, 100007 <https://doi.org/10.1016/j.srs.2020.100007>.
- Heidinger, A.K., Cao, C., Sullivan, J.T., 2002. Using Moderate Resolution Imaging Spectrometer (MODIS) to calibrate advanced very high resolution radiometer reflectance channels. *J. Geophys. Res. Atmos.* 107 <https://doi.org/10.1029/2001JD002035>.
- Ju, J., Roy, D.P., Vermote, E.F., Masek, J., Kovalsky, V., 2012. Continental-scale validation of MODIS-based and LEDAPS Landsat ETM+ atmospheric correction methods. *Remote Sens. Environ.* 122, 175–184. <https://doi.org/10.1016/j.rse.2011.12.025>.
- Kaufman, Y.J., 1987. Satellite sensing of aerosol absorption. *J. Geophys. Res.* 92, 4307. <https://doi.org/10.1029/JD092iD04p04307>.
- Kaufmann, R.K., Zhou, L., Knyazikhin, Y., Shabanov, N.V., Tucker, C.J., 2000. Effect of orbital drift and sensor changes on the time series of AVHRR vegetation index data. *IEEE Trans. Geosci. Remote Sens.* 38, 2584–2597. <https://doi.org/10.1109/36.885205>.
- Latifovic, R., Pouliot, D., Dillabaugh, C., 2012. Identification and correction of systematic error in NOAA AVHRR long-term satellite data record. *Remote Sens. Environ.* 127, 84–97. <https://doi.org/10.1016/j.rse.2012.08.032>.
- Lee, D.S., Storey, J.C., Choate, M.J., Hayes, R.W., 2004. Four years of Landsat-7 on-orbit geometric calibration and performance. *IEEE Trans. Geosci. Remote Sens.* 42, 2786–2795. <https://doi.org/10.1109/TGRS.2004.836769>.
- Li, C., Xue, Y., Liu, Q., Guang, J., He, X., Zhang, J., Wang, T., Liu, X., 2014. Post calibration of channels 1 and 2 of long-term AVHRR data record based on SeaWiFS data and pseudo-invariant targets. *Remote Sens. Environ.* 150, 104–119. <https://doi.org/10.1016/j.rse.2014.04.020>.
- Mahtab, A., Sridhar, V.N., Navalgund, R.R., 2009. An assessment of angular variations of red and NIR reflectances in multi-date IRS-1D Wide Field Sensor data. *Int. J. Remote Sens.* 30, 4599–4619. <https://doi.org/10.1080/01431160802621226>.
- Maignan, F., Bréon, F.M., Lacaze, R., 2004. Bidirectional reflectance of Earth targets: Evaluation of analytical models using a large set of spaceborne measurements with emphasis on the Hot Spot. *Remote Sens. Environ.* 90, 210–220. <https://doi.org/10.1016/j.rse.2003.12.006>.
- Markham, B.L., Helder, D.L., 2012. Forty-year calibrated record of earth-reflected radiance from Landsat: A review. *Remote Sens. Environ.* <https://doi.org/10.1016/j.rse.2011.06.026>.
- Masek, J.G., Vermote, E.F., Saleous, N.E., Wolfe, R., Hall, F.G., Huemmrich, K.F., Gao, F., Kutler, J., Lim, T., 2006. A Landsat Surface Reflectance Dataset. *IEEE Geosci. Remote Sens. Lett.* 3, 68–72. <https://doi.org/10.1109/LGRS.2005.857030>.
- Miura, T., Huete, A., Yoshioka, H., 2006. An empirical investigation of cross-sensor relationships of NDVI and red/near-infrared reflectance using EO-1 Hyperion data. *Remote Sens. Environ.* 100, 223–236. <https://doi.org/10.1016/j.rse.2005.10.010>.
- Pearlman, J.S., Barry, P.S., Segal, C.C., Shepanski, J., Beiso, D., Carman, S.L., 2003. Hyperion, a space-based imaging spectrometer. *IEEE Trans. Geosci. Remote Sens.* 41, 1160–1173. <https://doi.org/10.1109/TGRS.2003.815018>.
- Pérez-Hoyos, A., García-Haro, F.J.F., San-Miguel-Ayanz, J., 2012. Conventional and fuzzy comparisons of large scale land cover products: Application to CORINE,

- GLC2000, MODIS and GlobCover in Europe. ISPRS J. Photogramm. Remote Sens. 74, 185–201. <https://doi.org/10.1016/j.isprsjprs.2012.09.006>.
- Potapov, P.V., Turubanova, S.A., Tyukavina, A., Krylov, A.M., McCarty, J.L., Radeloff, V. C., Hansen, M.C., 2015. Eastern Europe's forest cover dynamics from 1985 to 2012 quantified from the full Landsat archive. Remote Sens. Environ. 159, 28–43. <https://doi.org/10.1016/j.rse.2014.11.027>.
- Roujean, J.L., Leroy, M., Deschamps, P.Y., 1992. A bidirectional reflectance model of the Earth's surface for the correction of remote sensing data. J. Geophys. Res. 97, 20455–20468. <https://doi.org/10.1029/92jd01411>.
- Skakun, S., Justice, C.O., Vermote, E.F., Roger, J.C., 2018. Transitioning from MODIS to VIIRS: an analysis of inter-consistency of NDVI data sets for agricultural monitoring. Int. J. Remote Sens. 39, 971–992. <https://doi.org/10.1080/01431161.2017.1395970>.
- Skakun, S., Kussul, N., Shelestov, A., Kussul, O., 2016. The use of satellite data for agriculture drought risk quantification in Ukraine. Geomatics. Nat. Hazards Risk 7, 901–917. <https://doi.org/10.1080/19475705.2015.1016555>.
- Song, X.P., Hansen, M.C., Stehman, S.V., Potapov, P.V., Tyukavina, A., Vermote, E.F., Townshend, J.R., 2018a. Global land change from 1982 to 2016. Nature. <https://doi.org/10.1038/s41586-018-0411-9>.
- Song, X.P., Hansen, M.C., Stehman, S.V., Potapov, P.V., Tyukavina, A., Vermote, E.F., Townshend, J.R., 2018b. Supplemental Material for Global land change from 1982 to 2016. Nature 560, 639–643. <https://doi.org/10.1038/s41586-018-0411-9>.
- Song, Z., Liang, S., Wang, D., Zhou, Y., Jia, A., 2018c. Long-term record of top-of-atmosphere albedo over land generated from AVHRR data. Remote Sens. Environ. 211, 71–88. <https://doi.org/10.1016/j.rse.2018.03.044>.
- Strahler, A., Muchoney, D., Borak, J., Friedl, M.A., Gopal, S., Lambin, E., Moody, A., 1999. MODIS Land Cover Product Algorithm Theoretical Basis Document (ATBD).
- Tange, O., 2011. GNU Parallel - The Command-Line Power Tool. login USENIX Mag. 36, 42–47. <https://doi.org/10.5281/zenodo.16303>.
- Van Leeuwen, W.J.D., Orr, B.J., Marsh, S.E., Herrmann, S.M., 2006. Multi-sensor NDVI data continuity: Uncertainties and implications for vegetation monitoring applications. Remote Sens. Environ. 100, 67–81. <https://doi.org/10.1016/j.rse.2005.10.002>.
- Vermote, E.F., Justice, C., Claverie, M., Franch, B., 2016. Preliminary analysis of the performance of the Landsat 8/OLI land surface reflectance product. Remote Sens. Environ. 185, 46–56. <https://doi.org/10.1016/j.rse.2016.04.008>.
- Vermote, E.F., Kaufman, Y.J., 1995. Absolute calibration of AVHRR visible and near-infrared channels using ocean and cloud views. Int. J. Remote Sens. 16, 2317–2340. <https://doi.org/10.1080/01431169508954561>.
- Vermote, E.F., Justice, C.O., Bréon, F.M., 2009. Towards a generalized approach for correction of the BRDF effect in MODIS directional reflectances. IEEE Trans. Geosci. Remote Sens. 47, 898–908. <https://doi.org/10.1109/TGRS.2008.2005977>.
- Vermote, E.F., Kotchenova, S.Y., 2008. Atmospheric correction for the monitoring of land surfaces. J. Geophys. Res. 113, D23S90. <https://doi.org/10.1029/2007JD009662>.
- Vermote, E.F., Saleous, N.Z., 2006a. Calibration of NOAA16 AVHRR over a desert site using MODIS data. Remote Sens. Environ. 105, 214–220. <https://doi.org/10.1016/j.rse.2006.06.015>.
- Vermote, E.F., Saleous, N.Z., 2006b. Operational atmospheric correction of modis visible to middle infrared land surface data in the case of an infinite lambertian target. In: Earth Science Satellite Remote Sensing: Science and Instruments. Springer, Berlin Heidelberg, pp. 123–153, 10.1007/978-3-540-37293-6 8.
- Vermote, E.F., Tanre, D., Deuze, J.L., Herman, M., Morcrette, J.J., 1997. Second Simulation of the Satellite Signal in the Solar Spectrum, 6S: An Overview. IEEE Trans. Geosci. Remote Sens. 35, 675–686.
- Villaescusa-Nadal, J.L., Franch, B., Roger, J.C., Vermote, E.F., Skakun, S., Justice, C., 2019a. Spectral Adjustment Model's Analysis and Application to Remote Sensing Data. IEEE J. Sel. Top. Appl. Earth Obs. Remote Sens. 12, 961–972. <https://doi.org/10.1109/JSTARS.2018.2890068>.
- Villaescusa-Nadal, J.L., Franch, B., Vermote, E.F., Roger, J.C., 2019b. Improving the AVHRR long term data record BRDF correction. Remote Sens. 11 <https://doi.org/10.3390/rs11050502>.
- Zhang, X., 2015. Reconstruction of a complete global time series of daily vegetation index trajectory from long-term AVHRR data. Remote Sens. Environ. 156, 457–472. <https://doi.org/10.1016/j.rse.2014.10.012>.